

**Enhanced Regional Ocean Ensemble Data Assimilation
Through Atmospheric Coupling in the SKRIPS Model**

Rui Sun¹, Sivareddy Sanikommu², Aneesh C. Subramanian³, Matthew R. Mazloff¹, Bruce D. Cornuelle¹, Ganesh Gopalakrishnan¹, Arthur J. Miller¹, Ibrahim Hoteit²

¹Scripps Institution of Oceanography, California, USA

²Physical Sciences and Engineering Division, King Abdullah University of Science and Technology

(KAUST), Thuwal, Saudi Arabia

³Department of Atmospheric and Oceanic Sciences, University of Colorado Boulder, Colorado, USA

10 **Abstract**

11 We investigate the impact of ocean data assimilation using the Ensemble Adjustment
 12 Kalman Filter (EAKF) from the Data Assimilation Research Testbed (DART) on the
 13 oceanic and atmospheric states of the Red Sea. Our study extends the ocean data as-
 14 similation experiment performed by Sanikommu et al. (2020) by utilizing the SKRIPS
 15 model coupling the MITgcm ocean model and the Weather Research and Forecasting (WRF)
 16 atmosphere model. Using a 50-member ensemble, we assimilate satellite-derived sea sur-
 17 face temperature and height and in-situ temperature and salinity profiles every three days
 18 for one year, starting January 01 2011. Atmospheric data are not assimilated in the ex-
 19 periments. To improve the ensemble realism, perturbations are added to the WRF model
 20 using several physics options and the stochastic kinetic energy backscatter (SKEB) scheme.
 21 Compared with the control experiments using uncoupled MITgcm with ECMWF ensem-
 22 ble forcing, the EAKF ensemble mean oceanic states from the coupled model are bet-
 23 ter or insignificantly worse (root-mean-square errors are 30% to -2% smaller), especially
 24 when the atmospheric model uncertainties are accounted for with stochastic perturba-
 25 tions. We hypothesize that the ensemble spreads of the air-sea fluxes are better repre-
 26 sented in the downscaled WRF ensembles when uncertainties are well accounted for, lead-
 27 ing to improved representation of the ensemble oceanic states from the new experiments
 28 with the coupled model. This indicates the ocean model assimilation will be improved
 29 with coupled models and relaxes the need for operational centers to provide atmospheric
 30 ensembles to drive ocean forecasts. Although the feedback from ocean to atmosphere is
 31 included in this two-way regional coupled configuration, we find no significant effect of
 32 ocean data assimilation on the ensemble mean latent heat flux and 10-m wind speed over
 33 the Red Sea. This suggests that the improved skill using the coupled model is not from
 34 the two-way coupling, but from downscaling the ensemble atmospheric forcings (one-way
 35 coupled) to drive the ocean model.

36 **Plain Language Summary**

37 We investigate how combining ocean information accounting for weather processes
 38 can help us better understand and predict the ocean-atmospheric state of the Red Sea.
 39 We use a coupled ocean and atmosphere model to assimilate satellite and ship-based ocean
 40 observations. We assess the performance of the assimilation system using fifty different
 41 realizations of the atmospheric state and found that it improves the prediction of oceanic
 42 state compared to using the ocean model alone for assimilation and prediction. This suc-
 43 cess is because the combined ocean-atmosphere model provides a broader range of pos-
 44 sible ocean conditions. We also look at how incorporating ocean observation informa-
 45 tion may potentially impact weather forecasts in the coupled model.

46 **1 Introduction**

47 Numerical models have been used to analyze and predict ocean states for decades.
 48 Realistically configured numerical models can simulate oceanic conditions that are gen-
 49 erally consistent with observations, but there can be substantial differences when com-
 50 paring with observations at specific times and locations (Edwards et al., 2015). Even with
 51 a perfect model, the differences can result from uncertainties of initial conditions, per-
 52 turbations, parameterizations, and forcings. Because of this, data assimilation (DA) is
 53 used to constrain the model solutions using observational data, including observation un-
 54 certainty and model representational error (Edwards et al., 2015).

55 The Ensemble Kalman Filter (hereafter EnKF) provides an efficient framework for
 56 ocean data assimilation (Evensen, 1994). It has gained popularity because of its simple
 57 conceptual formulation and relative ease of implementation, requiring no derivation of
 58 tangent linear or adjoint models, with only forward model integration in time (Evensen,
 59 2003). Furthermore, its computational requirements scale with ensemble size, and so can

60 be affordable and comparable with other popular sophisticated assimilation methods (Evensen,
 61 2003). EnKF based data assimilation systems have been developed for many applica-
 62 tions. For example, Evensen and Van Leeuwen (1996) assimilated altimeter data in the
 63 Agulhas region using a quasi-geostrophic model; Sakov et al. (2012) and Hoteit et al. (2013)
 64 respectively produced realistic estimates of the ocean circulation in the North Atlantic
 65 and the Gulf of Mexico; Sanikommu et al. (2020) investigated the impact of atmospheric
 66 forcing and model physics perturbations using an Ensemble Adjustment Kalman Filter (EAKF).
 67 In addition to ocean data assimilation, EnKF is used for operational atmospheric assim-
 68 ilation at the Canadian Meteorological Centre (Houtekamer et al., 2005) among many
 69 other applications (e.g., Lawson & Hansen, 2004; Leeuwenburgh et al., 2005; Bannister,
 70 2017).

71 A major component of EnKF data assimilation systems is the background error
 72 covariance estimated from the ensembles (Bannister, 2008a, 2008b; Song et al., 2010).
 73 EnKFs can suffer from the collapse of the ensemble spread, which unrealistically reduces
 74 the background error covariance in the data assimilation system (e.g., J. Anderson & An-
 75 derson, 1999; Hoteit et al., 2002). This is often mitigated using covariance inflation tech-
 76 niques to increase the ensemble spread to better describe the background covariance (J. An-
 77 derson & Anderson, 1999; Hoteit et al., 2002; F. Zhang et al., 2004; Whitaker & Hamill,
 78 2012; Luo & Hoteit, 2012). A more representative approach is to account directly for un-
 79 certainties in the model, such as the forcing and boundary conditions. Diverse high-resolution
 80 forcings that represent the uncertainty of the atmosphere are indeed desirable for ocean
 81 ensemble data assimilation system. Many studies have demonstrated improved forecasts
 82 and analyses when driving ensemble ocean data assimilation systems with perturbed at-
 83 mospheric forcing (Lisæter et al., 2003; Evensen, 2004; Wan et al., 2008; Shu et al., 2011;
 84 Sakov et al., 2012; Karspeck et al., 2013; Penny et al., 2015; Sanikommu et al., 2017, 2019).
 85 Others investigated the perturbed model physics (Sandery et al., 2014; Brankart et al.,
 86 2015; Lima et al., 2019), or combined the perturbations of atmospheric forcing and model
 87 physics (Vandenbulcke & Barth, 2015; K. M. Kwon et al., 2016; Sanikommu et al., 2020).
 88 A recent study by Sanikommu et al. (2020) performed a detailed analysis of the impacts
 89 of model physics perturbations and atmospheric forcing on a high-resolution regional ocean
 90 DA system. The DA experiments improved the forecasts of oceanic states by using mul-
 91 tiple oceanic model physics and ensemble atmospheric forcing now available from oper-
 92 ational weather systems.

93 Our study takes a step forward toward a fully coupled ocean–atmospheric data as-
 94 similation system, with application to the Red Sea region. A regional assimilation sys-
 95 tem is crucial for improving forecasts in the Red Sea due to its unique characteristics in
 96 terms of both oceanic and atmospheric conditions (Hoteit et al., 2021). The region is prone
 97 to dust and sandstorms, particularly during the transitional seasons of spring and au-
 98 tumn, originating from nearby deserts like the Sahara. These storms significantly reduce
 99 visibility and impact air quality (Prakash et al., 2014). The Red Sea also experiences fre-
 100 quent temperature inversions, especially in winter, which affect temperature profiles, pol-
 101 lutant dispersal, and vertical mixing of air masses. The region is influenced by two pri-
 102 mary wind patterns: the Southwest Monsoon, bringing humid air and thunderstorms,
 103 and the Northwest Monsoon, bringing drier air (Langodan et al., 2017). A sea breeze
 104 often develops during the day, cooling coastal areas (Davis et al., 2019). The Red Sea
 105 warm surface waters contribute to high levels of water vapor, impacting local weather
 106 conditions and precipitation. The local atmospheric features vary significantly with sea-
 107 sons, weather patterns, and local geography (Dasari et al., n.d.). The Red Sea holds eco-
 108 nomic importance and plays a vital role in international trade. Further, the Red Sea cir-
 109 culation plays a dominant role in modifying the salinity budgets of the western Indian
 110 Ocean. Global reanalysis often fails to capture the Red Sea circulation features accurately
 111 due to coarse resolutions and limited observations (Sanikommu et al., 2023a). Develop-
 112 ing a high-resolution regional reanalysis using local observations and coupled ocean–atmospheric

113 data assimilation system would greatly enhance the forecasts in the Red Sea, and this
 114 is important for many applications in this unique region.

115 In this context, we implement a new ensemble DA system for the Red Sea using
 116 the Scripps–KAUST Regional Integrated Prediction System (SKRIPS, Sun et al., 2019,
 117 2023) and the Data Assimilation Research Testbed (DART, J. Anderson et al., 2009).
 118 This work is an extension of previous DA efforts for the Red Sea (Toye et al., 2017; Sanikommu
 119 et al., 2020, 2023b), replacing the uncoupled ocean model with the SKRIPS coupled model (Sun
 120 et al., 2019, 2023). Here we assimilate only oceanic observations using the DART–EAKF
 121 system and investigate the estimated oceanic and atmospheric states of the Red Sea re-
 122 gional coupled model, using different options to perturb the physics of the atmosphere
 123 model. We evaluate the performance of the coupled model in forecasting the oceanic states,
 124 the impact of atmospheric model physics options on the coupled model, and the feed-
 125 back of the ocean data assimilation to the atmospheric model. Although we only assim-
 126 ilate ocean observations in this work, the present study is a step toward developing a weakly
 127 coupled DA system and operational analysis and forecasting system for the Red Sea. Be-
 128 cause the random atmospheric states are generated by perturbing the model physics when
 129 using a coupled model, there is less need to generate large ensembles of atmospheric forc-
 130 ings (Sanikommu et al., 2023a), enhancing the robustness of the DA system.

131 The rest of the manuscript is organized as follows. We first introduce the ensem-
 132 ble DA system and its implementation in Section 2. The results of the DA experiments
 133 are presented and discussed in Section 3. The final section outlines the main findings and
 134 concludes this work.

135 2 Implementations and Experimental Design

136 2.1 The Data Assimilation Framework

137 We use the SKRIPS model (Sun et al., 2019) for the coupled simulation: the oceanic
 138 model component is the MIT general circulation model (MITgcm, Marshall et al., 1997;
 139 Campin et al., 2019) and the atmospheric model component is the Weather Research and
 140 Forecasting (WRF) model (Skamarock et al., 2019). The Earth System Modeling Frame-
 141 work (ESMF, Hill et al., 2004) and the National United Operational Prediction Capa-
 142 bility (NUOPC) layer are used to handle the coupling between MITgcm and WRF. The
 143 schematic diagram of the DART–SKRIPS framework and the domain used in the exper-
 144 iment are shown in Fig. 1. The ocean data are assimilated using EAKF available from
 145 the DART–MITgcm package (Hoteit et al., 2013, 2015), aiming to evaluate their impact
 146 on the ocean and atmosphere states in the coupled system. The ROCOTO workflow (Harrop
 147 et al., 2017) is used for the management of the pre- and post-processing scripts in the
 148 developed DART–SKRIPS framework.

149 The coupled model is also described in the diagram shown in Fig. 1. In the cou-
 150 pling process, MITgcm sends sea surface temperature (SST) and ocean surface veloc-
 151 ity to WRF; WRF sends air-sea flux and surface atmospheric fields to MITgcm, includ-
 152 ing (1) net surface longwave and shortwave radiative fluxes, (2) surface latent and sen-
 153 sible heat fluxes, (3) 10-m wind speed, (4) precipitation, and (5) evaporation. The MIT-
 154 gcm model uses the surface atmospheric variables to prescribe surface forcing, includ-
 155 ing (1) total net surface heat flux, (2) surface wind stress, and (3) freshwater flux. The
 156 total net surface heat flux is computed by adding surface latent heat flux, sensible heat
 157 flux, net shortwave radiation flux, and net longwave radiation flux. The surface latent
 158 and sensible heat fluxes are computed using the COARE 3.0 bulk algorithm in WRF (Fairall
 159 et al., 2003).

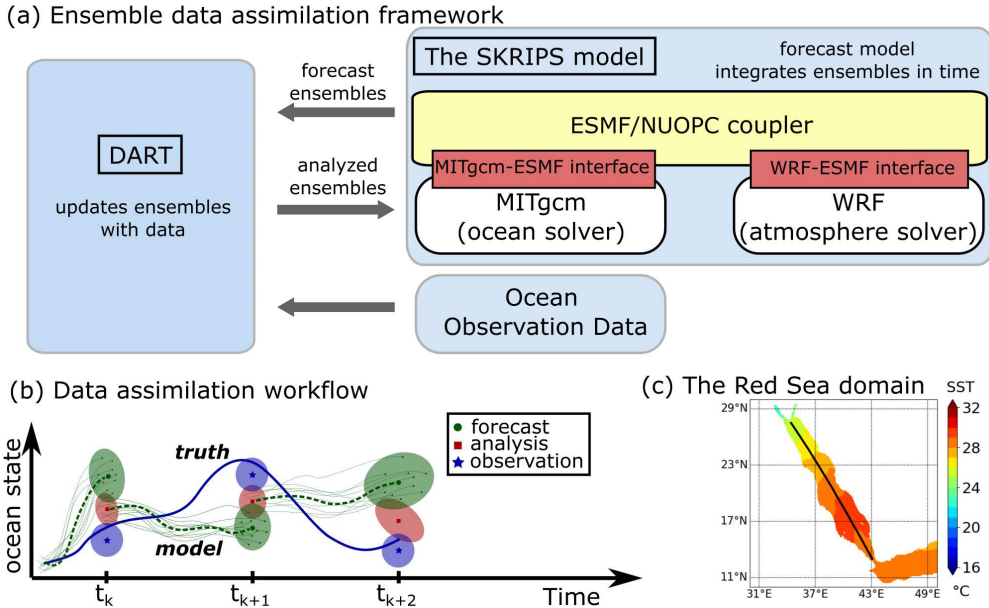


Figure 1. The schematic description of the DART–SKRIPS data assimilation system.

Panel (a) indicates the DART–SKRIPS framework: the blue blocks denote the SKRIPS model, DART, and ocean observations; the yellow block is the ESMF/NUOPC coupler; the white blocks are the ocean and atmosphere components; the red blocks are the implemented MITgcm–ESMF and WRF–ESMF interfaces. The arrows indicate the information exchange between DART and SKRIPS. Panel (b) shows the workflow at three time steps: the thick solid line indicates the evolution of the “truth”; the dashed line indicates the ensemble averaged forecast; the thin solid lines indicate the evolution of the ensemble members; the red dots indicate the analysis; the shaded areas indicate the error covariance; t_k , t_{k+1} , and t_{k+2} indicate three steps when observational data are assimilated. Panel (c) shows the domain of the coupled model, with the black line indicating the centerline of the Red Sea.

160 2.2 Experimental Design

161 To study the impact of ocean data assimilation on the oceanic and atmospheric states,
 162 we perform a series of 50-member ensemble DA experiments using coupled and un-
 163 coupled models starting from January 01 2011, assimilating the observational data every 3
 164 days. For the coupled model experiments, the ocean and atmosphere models are nested
 165 in GLORYS and ERA5 reanalyses, respectively. For the uncoupled model experiments,
 166 the ocean model is also nested in GLORYS, but driven by ECMWF derived atmospheric
 167 forcing. Further details on the initial and boundary conditions will be discussed in the
 168 latter sections. The same setup is used for the ocean model, but different options are used
 169 for the atmosphere in the 50-member ensemble DA experiments:

- 170 1. OCN.daO uses only the ocean model forced by the ECMWF ensemble mean.
- 171 2. OCN.daF uses only the ocean model forced by the 50-member ECMWF ensem-
 172 bles.
- 173 3. CPL.daO uses the coupled model with no perturbations to the atmosphere.
- 174 4. CPL.daS uses the coupled model with stochastic forcings in the atmospheric model.
- 175 5. CPL.daP uses the coupled model with perturbed physics options in the atmospheric
 176 model (e.g., microphysics, convection, and planetary boundary layer).
- 177 6. CPL.daSP uses the coupled model with stochastic forcings and perturbed atmo-
 178 sphere physics options.

179 OCN.daO and OCN.daF follow the experiments using the ocean-only models in Sanikommu
 180 et al. (2020), but without inflation to investigate the changes using the coupled model.
 181 They also serve as benchmarks to evaluate the performance of the coupled experiments.
 182 In the coupled DA experiment CPL.daO, although we did not perturb the atmospheric
 183 model physics, the randomness of the atmospheric forcing is from the feedback of dif-
 184 ferent ocean states. Different random seeds are used for the stochastic model in CPL.daS
 185 and CPL.daSP from 1 to 50. The coupled DA experiments OCN.daS, OCN.daP, and OCN.daSP
 186 are conducted to assess the effect of different strategies of the atmospheric forcings, and
 187 thus we did not assimilate the atmospheric observational data in our experiments. Al-
 188 though the ocean feedback is important in the coupled model, we did not perform DA
 189 experiments driven by the atmospheric forcings from stand-alone WRF models because
 190 it is out of the scope of our work.

191 2.3 The Forward Models

192 The initial conditions, boundary conditions, and forcings are outlined in Table 1.
 193 The MITgcm initial conditions are obtained from a spin-up run as described in Sanikommu
 194 et al. (2020), with randomly selecting 50 ocean states corresponding to ± 15 days from
 195 the initial time. The boundary conditions for the ocean are updated by linearly inter-
 196 polating between the daily data from Global Ocean Reanalysis and Simulation (GLORYS,
 197 Jean-Michel et al., 2021). For the uncoupled experiments, the atmospheric forcings are
 198 from the ECMWF atmospheric ensemble from The Observing System Research and Pre-
 199 dictability Experiment Interactive Grand Global Ensemble project (TIGGE, Bougeault
 200 et al., 2010), with full details available in Buizza (2014). We combined the fields of the
 201 00 and 12 UTC TIGGE initial conditions and 06 and 18 UTC forecasts as 6-hourly forc-
 202 ing for our ocean ensemble assimilation runs. For OCN.daO, we forced the model with
 203 the ensemble mean of the atmospheric forcings; for OCN.daF, we forced the model with
 204 the ECMWF 50-member ensembles. In the coupled experiments, ERA5 provides the ini-
 205 tial and boundary conditions for the atmosphere model, with the atmospheric bound-
 206 ary conditions updated by linearly interpolating between the 6-hourly fields. Spectral
 207 nudging is not used in the DA experiments because (1) nudging may constrain the high
 208 frequency internal variability of the atmosphere model and (2) the domain size is com-
 209 parable with wavelengths typically used in the spectral nudging simulations (Liu et al.,
 210 2012).

211 We choose the latitude–longitude (cylindrical equidistant) map projection to gen-
 212 erate the grids for MITgcm and WRF. The domains for both models extend from 10°N
 213 to 30°N and from 30°E to 50°E. In the ocean model, the horizontal grid has 500×500
 214 (lat \times long) cells and the spacing is about 4 km; in the atmospheric model, the hori-
 215 zontal grid has 125×125 (lat \times long) cells and the spacing is about 16 km. There are 40 sigma
 216 layers in the atmospheric model (top pressure is 50 hPa) and 50 z-layers in the ocean
 217 model ($dz = 4$ m at the top). The time step of the oceanic model is 200 seconds; the
 218 time step of the atmospheric model is 25 seconds; the coupling interval is 200 seconds.

219 2.4 Model Perturbations

220 For the oceanic simulations in all DA experiments, we use various physical param-
 221 eterization schemes to account for the effects of unresolved scales of motion as proposed
 222 by Sanikommu et al. (2020), summarized in Table 2. Three different categories of model
 223 physics are selected: horizontal viscosity, vertical mixing, and horizontal diffusion. We
 224 include three different horizontal viscosity schemes: the simple harmonic scheme, the sim-
 225 ple biharmonic of Holland (1978), and the Smagorinsky/Leith scheme (Smagorinsky et
 226 al., 1993; Griffies & Hallberg, 2000) with the coefficients suggested in the literature (Leith,
 227 1996; Griffies & Hallberg, 2000). For vertical mixing, four different schemes are included:
 228 the nonlocal K-Profile Parameterization (KPP) scheme (W. G. Large et al., 1994), the
 229 PP81 scheme (Pacanowski & Philander, 1981), the MY82 scheme (Mellor & Yamada,

1982), and the GGL90 scheme (Gaspar et al., 1990). For the horizontal diffusion, we use implicit diffusion, simple-explicit harmonic diffusion, and three different flavors of Gent-McWilliams/Redi subgrid-scale eddy parameterization schemes (hereafter GMREDI, Gent & Mcwilliams, 1990; Gent et al., 1995; Redi, 1982): the GMREDI clipping scheme of Cox (1987), the GMREDI-dm95 tapering scheme of Danabasoglu and McWilliams (1995), and the GMREDI-ldd92 tapering scheme of W. Large et al. (1997). Table 2 lists the coefficients used in these schemes.

We also perturb the physics options in WRF to parameterize microphysics, convection, and planetary boundary layer (PBL), summarized in Table 3. For the micro-physics we use the Morrison 2-moment scheme (Morrison et al., 2009), the Purdue-Lin scheme (Chen & Sun, 2002), the Thompson scheme (Thompson et al., 2008), the WRF single moment 6-class scheme (Hong & Lim, 2006), and the WRF double moment 6-class scheme (Lim & Hong, 2010). For the cumulus convection, we use the Kain–Fritsch scheme (Kain, 2004), the Betts–Miller–Janjic scheme (Janjić, 1994), the Grell–Freitas Ensemble scheme (Grell & Freitas, 2014), the new Tiedtke scheme (C. Zhang & Wang, 2017), and the simplified Arakawa–Schubert scheme (Y. C. Kwon & Hong, 2017). For the planetary boundary layer, we use the Mellor–Yamada Nakanishi Niino scheme (MYNN, Nakanishi & Niino, 2004, 2009), the Yonsei University scheme (Hong et al., 2006), and the Mellor–Yamada–Janjic scheme (Janjić, 1994). The radiation and land surface schemes are not perturbed: the Rapid Radiation Transfer Model for GCMs (RRTMG, Iacono et al., 2008) is used for long-wave and shortwave radiation transfer through the atmosphere; the Noah land surface model is used for the land surface processes (Tewari et al., 2004). The physics scheme perturbation is based on the ensemble forecast system of the Center For Western Weather and Water Extremes (CW3E, Oakley et al., 2023). For the experiments without perturbing the atmospheric model (i.e., CPL.daO and CPL.daS), we use Morrison 2-moment scheme, Kain–Fritsch scheme, and MYNN scheme for microphysics, convection, and PBL, respectively.

In addition to perturbing the atmospheric model physics, we used the SKEB scheme (Shutts, 2005; Berner et al., 2009) to account for the unrepresented uncertainties in the model. This scheme adds stochastic, small-amplitude perturbations to the horizontal wind and potential temperature. The default amplitudes of the stochastic perturbations in WRF were used in CPL.daS and CPL.daSP, which were able to provide more reliable ensemble spreads (Berner et al., 2011, 2015).

2.5 Data Used in Assimilation and Validation

We assimilate data from level-4 SST blended daily product available on a $0.25^\circ \times 0.25^\circ$ grid (Reynolds et al., 2007; Banzon et al., 2016), along-track satellite altimeter level-3 sea level anomalies (SLAs; corrected for dynamic atmospheric loading, ocean tide, and long wavelength errors) available from Copernicus Marine Environment Monitoring Service (here after CMEMS-L3, Mertz et al., 2017), and quality controlled in situ glider temperature and salinity profiles from EN4 data (Ingleby & Huddleston, 2007; Good et al., 2013). The in situ temperature and salinity profiles are sparse, and there are only 244 temperature and 110 salinity profiles in the entire year 2011 from the glider in the Red Sea. Errors associated with these observations are assumed uncorrelated, so the observational error covariance matrix is diagonal. The combined observation and representation error variance is determined based on previous DA experiments (Toye et al., 2017; Sanikommu et al., 2020) and accounts for errors due to: measurement devices, omitted processes, unresolved subgrid scale dynamics, and numerical errors in interpolation. Temporally static, partially homogeneous, and depth independent observational error variance values of $(0.5^\circ\text{C})^2$, $(0.04 \text{ m})^2$, $(0.5^\circ\text{C})^2$, and $(0.3 \text{ psu})^2$ are then used for satellite SST, satellite along-track SLA, in situ temperature and salinity, respectively. A cutoff radius of about 300 km was imposed to localize the impact the observations in the horizontal directly (not in the vertical) as a way to mitigate spurious correlations.

Table 1. The computational domain, WRF physics schemes, initial condition, boundary condition, and forcing terms used in the present simulations.

	OCN Experiments	CPL Experiments
Model region	10°N to 30°N; 30°E to 50°E	
Grid size	500×500	500×500 for ocean 125×125 for atmosphere
Grid spacing	0.04° × 0.04°	0.04° × 0.04° for ocean 0.16° × 0.16° for atmosphere
Microphysics scheme		Various (see Table 3)
Convection scheme		Various (see Table 3)
PBL scheme	Not necessary	Various (see Table 3)
Longwave radiation scheme		RRTMG
Shortwave radiation scheme		RRTMG
Land surface scheme		Noah land surface model
Vertical levels	50 (ocean only)	40 (atmosphere) 50 (ocean)
Initial and boundary conditions	GLORYS (ocean only)	ERA5 (atmosphere) GLORYS (ocean)
Atmospheric forcings for oceanic model	From ECMWF TIGGE product	From WRF

Table 2. MITgcm model physics parameterizations in the present study.

Horizontal Viscosity	Vertical Mixing	Horizontal Diffusion
Simple Harmonic (30 m ² /s)	K-Profile Parameterization	Implicit Diffusion
Simple Biharmonic (10 ⁷ m ⁴ /s)	PP81	Explicit Diffusion (100 m ² /s)
SMAGLEITH-Harmonic (30 m ² /s), Smag Coeff 2.5, and Leith Coeff 1.85	MY82 GGL90	GMREDI-clipping (100 m ² /s) GMREDI-dm95 (100 m ² /s) GMREDI-dd92 (100 m ² /s)

Table 3. WRF model physics parameterizations in the present study. The physics options used in the experiments without perturbing the model physics (i.e., CPL.daO and CPL.daS) are highlighted using bold red color.

Microphysics	Convection	Planetary Boundary Layer
Morrison 2-moment	Kain–Fritsch	Mellor–Yamada Nakanishi Niino
Purdue–Lin	Bettis–Miller–Janjic	Yonsei University
Thompson	Grell–Freitas Ensemble	Mellor–Yamada–Janjic
WRF single moment 6-class	New Tiedtke	
WRF double moment 6-class	Simplified Arakawa–Schubert	

282 For validation, we evaluate the daily averaged ocean forecasts and analyses as re-
 283 sulting from the DA experiments. We first use the assimilated data to examine the time
 284 series of innovations and residuals. In addition to the assimilated data, independent ob-
 285 servations are used. To analyze the subsurface features, we use 206 profiles of temper-
 286 ature and salinity collected between September 15 to October 08 2011 by a joint Woods
 287 Hole Oceanography Institute (WHOI) and King Abdullah University of Science and Tech-
 288 nology (KAUST) cruise along the eastern part of the Red Sea, collected with a horizon-
 289 tal spacing of 10 km (Zhai et al., 2015). We also use other satellite products to eval-
 290 uate the DA results. For SST we select the high-resolution daily averaged level 4 SST prod-
 291 uct from the Operational Sea Surface Temperature and Sea Ice Analysis (OSTIA, Stark
 292 et al., 2007; Donlon et al., 2012) because it is mapped differently with higher resolution.
 293 For sea surface height (SSH) we use multimission altimeter merged satellite level 4 grid-
 294 ded absolute dynamic topography (ADT) provided by CMEMS (hereafter CMEMS-L4,
 295 Mertz et al., 2017). Compared with the assimilated CMEMS-L3 data, the CMEMS-L4
 296 data is gridded on a 0.25° grid and thus can be used to estimate the errors across the
 297 entire Red Sea region. The SSH anomaly from the DA experiments is the instantaneous
 298 SSH obtained in the simulations minus the time-averaged SSH from the 15-year MIT-
 299 gcm model in Sanikommu et al. (2020). The SSH anomalies in CMEMS-L3 and CMEMS-
 300 L4 are the sea level height above the mean surface based on the long-term averaged ob-
 301 servations between 1993 to 2012. Because of the lack of in situ observational data of the
 302 atmosphere, we use ERA5 to validate the latent heat fluxes and wind speed simulated
 303 by the coupled experiments.

3 Results

305 The results obtained from the DA experiments are presented in this section. First,
 306 we analyze the ensemble spread of the atmospheric forcings and sea surface temperature.
 307 Then we examine the ocean states (e.g., SST, SSH, and vertical profiles) to assess the
 308 impact of atmospheric forcings in the uncoupled and coupled systems using the valida-
 309 tion data. In addition to the ocean states, the air-sea exchanges (e.g., latent heat flux)
 310 and surface atmospheric states (e.g., wind speed) are also analyzed to illustrate the feed-
 311 back from the ocean to the atmosphere due to assimilation. Finally, we discuss the changes
 312 in the ocean dynamics from assimilating the observation data.

3.1 Ensemble Spread Analysis

313 Similarly to the DA experiments in Sanikommu et al. (2020), we hypothesize that
 314 the estimated ocean states are improved when uncertainties in various sources are well
 315 accounted for. Incorporating uncertainties in the system improves ensemble spreads in
 316 the ocean systematically. For instance, Figs. 2 and 3 display the temporal evolution of
 317 atmospheric forcing root-mean-square (RMS) spread in the DA experiments, except for
 318 OCN.daO which is forced by the ECMWF ensemble mean. The spread in OCN.daF is
 319 from the ECMWF ensemble atmospheric forcing; others are from the coupled model out-
 320 puts. In comparison with OCN.daF, the spread in CPL.daO is smaller by about one or-
 321 der of magnitude because the atmospheric models are not perturbed and the spread of
 322 atmosphere is from the ocean perturbations. When the SKEB scheme is applied in CPL.daF
 323 and CPL.daSP, the spread of the atmospheric forcing is larger than that in OCN.daF,
 324 which in turn increases the SST spread, shown in Fig. 4. The impact of the atmospheric
 325 forcings on the ocean states will be detailed in the latter sections.

3.2 Sea Surface Temperature

326 We analyze the SST obtained in our DA experiments to assess its sensitivity to the
 327 atmospheric perturbations. The root-mean-square-errors (RMSEs) between the SST anal-
 328 yses and observations in all DA experiments are shown in Fig. 5 and summarized in Ta-

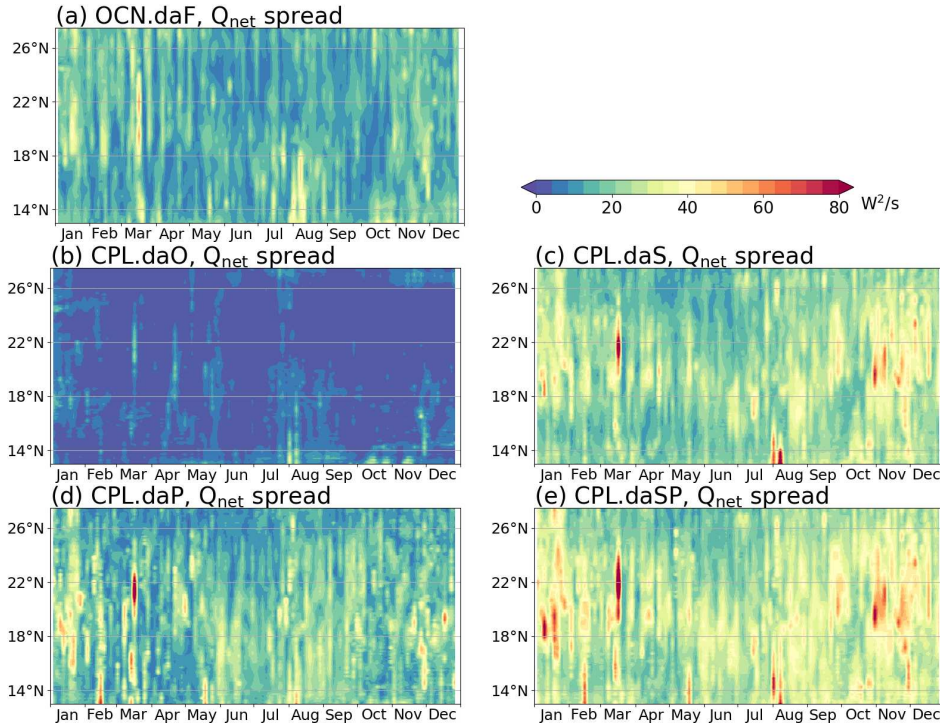


Figure 2. The spatial and temporal evolution of the RMS spread of net surface heat flux Q_{net} along the center line of the Red Sea shown in Fig. 1(c). The Q_{net} is calculated by summing up the latent heat flux, sensible heat flux, net surface shortwave fluxes, and net surface longwave fluxes. Panel (a) shows the spread in the ocean-only experiment driven by ECMWF derived forcing; Panel (b-e) show the spread in the coupled experiments with no perturbations, only SKEB, only perturbed model physics, and SKEB + perturbed model physics, respectively.

ble 4. The best SST forecast and analysis are both from experiment CPL.daSP, when the SKEB scheme is turned on and the WRF physics options are perturbed. The SSTs obtained in the coupled experiments (CPL.daS, CPL.daP, and CPL.daSP; except for the benchmark case CPL.daO) are better than that of the uncoupled experiment OCN.daF, with improvements more than twice larger than standard error of the mean SST from CPL.daSP (about 0.015°C , the standard deviation of SST divided by the square-root of the number of ensemble members). Better improvements are obtained when using only the stochastic forcings (CPL.daS) compared with only perturbing the WRF physics (CPL.daP), but this difference is less significant (smaller than 0.015°C). Although the perturbations in the atmospheric forcing are small in CPL.daO (shown in Figs. 2 and 3), the RMSE errors of SST forecasts and analyses are improved compared to the benchmark experiment OCN.daO by 0.156°C and 0.101°C , respectively. This indicates that small perturbations of the atmospheric forcing can improve SST in the DA experiments.

Figure 5 shows that the RMSEs of SST forecasts and analyses increase in summer for the benchmark runs (i.e., OCN.daO and CPL.daO), but RMSEs get smaller when using the coupled model (i.e., CPL.daS, CPL.daP, and CPL.daSP). In this season, the SST has a larger spread in all the experiments, similar to the results shown in Sanikommu et al. (2020), likely because the ocean is more sensitive to heat fluxes when the mixed layer depth is shallower.

In addition to the assimilated data, we validated the SSTs using the OSTIA SST. The RMSEs and correlations are shown in Fig. 6 and summarized in Table. 4. We present the SST correlations to evaluate the forecast of the SST evolution during the year. It can be seen that the SST obtained in CPL.daSP has larger correlations and smaller RM-

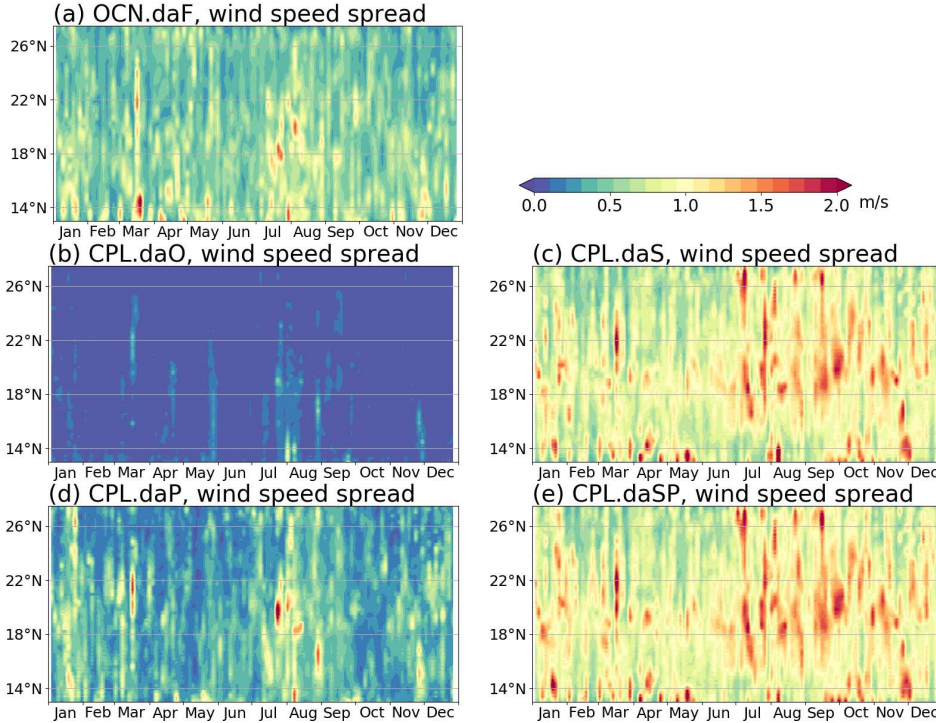


Figure 3. The spatial and temporal evolution of the RMS spread of 10-m wind speed along the center line of the Red Sea shown in Fig. 1(c). Panel (a) shows the spread from the ECMWF derived forcing; Panel (b-e) show the spread in the coupled experiments with no perturbations, only SKEB, only perturbed model physics, and SKEB + perturbed model physics, respectively.

SEs in the north Red Sea, center Red Sea, and Gulf of Aden regions. Compared with the uncoupled experiment OCN.daF, the coupled experiment CPL.daSP has a smaller RMSE by 0.035°C (6.5%, more than twice the standard error). On the other hand, the SST analysis obtained in CPL.daSP has a slightly larger RMSE compared to that obtained in CPL.daF, but the differences between OCN.daF, CPL.daS, CPL.daP, and CPL.daSP are within 0.01°C (2%). In addition, the CPL.daSP also has the smallest distance between the forecasts and analyses RMSEs, indicating less “assimilation shock” and more balanced ocean states in the DA experiment.

3.3 Sea Surface Height

The SSH fields as estimated in the DA experiments are presented in Fig. 7 and Table 5. Similar to the SST results, the coupled DA experiments exhibit smaller RMSE and larger spread. The SSH forecast errors in OCN.daF, CPL.daS, CPL.daP, and CPL.daSP are not significantly different. Although CPL.daSP still has the smallest RMSEs, the differences are within 1% and smaller than the standard errors (about 0.001 m). For the SSH analyses, on the other hand, the CPL.daS and CPL.daSP are more significantly improved (RMSEs are smaller by 10% compared with OCN.daF and CPL.daP) when SKEBS are used, suggesting that including the stochastic forcing in model parameters is the key for improvements. Note that the spread of surface wind forcing shown in Fig. 3 is greatly increased when using the stochastic forcing.

The temporal evolution of the SSH is also examined by comparing with CMEMS-L4 data, shown in Fig. 8. Here we only highlight the differences of the SSH analyses because the forecasts are close to each other. Figure. 8 shows that the CPL.daSP experiment has larger correlations and smaller RMSEs in both the Red Sea and the Gulf of Aden regions. Similar to the results shown in Fig. 7, when using the stochastic forcings

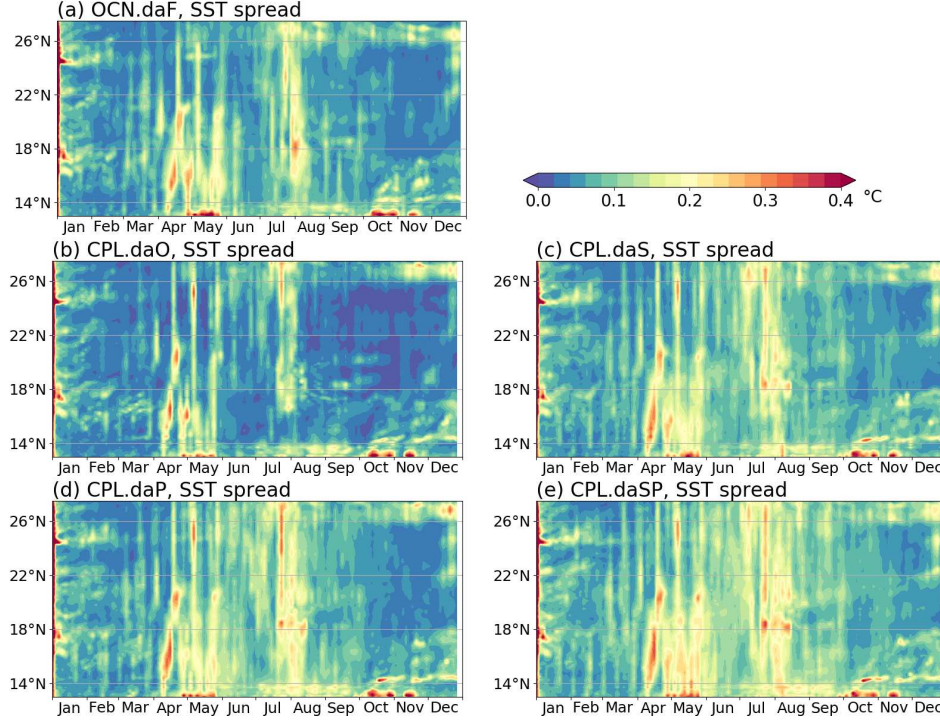


Figure 4. The spatial and temporal evolution of the RMS spread of Sea Surface Temperature along the center line of the Red Sea shown in Fig. 1(c). Panel (a) shows the spread in the ocean-only experiment driven by ECMWF derived forcing; Panel (b-e) show the spread in the coupled experiments with no perturbations, only SKEB, only perturbed model physics, and SKEB + perturbed model physics, respectively.

Table 4. SST obtained in the DA experiments against the validation data. We highlighted the best forecast/analysis using red, but the pink color is used when the differences between uncoupled and coupled experiments are insignificant (when the RMSE difference is smaller than 5% or the standard error).

	OCN.daO	OCN.daF	CPL.daO	CPL.daS	CPL.daP	CPL.daSP
Against assimilated data						
SST forecast RMSE	0.656	0.486	0.500	0.419	0.426	0.403
SST analysis RMSE	0.475	0.341	0.374	0.281	0.294	0.262
Against OSTIA SST						
SST forecast RMSE	0.650	0.574	0.610	0.560	0.551	0.539
SST analysis RMSE	0.486	0.463	0.484	0.468	0.472	0.469
SST forecast correlation	0.9580	0.9623	0.9573	0.9637	0.9628	0.9649
SST analysis correlation	0.9786	0.9805	0.9773	0.9800	0.9788	0.9791
SST forecast spread	0.078	0.080	0.077	0.098	0.095	0.108
SST analysis spread	0.046	0.052	0.048	0.059	0.055	0.062

in WRF, CPL.daS and CPL.daSP outperform the uncoupled model OCN.daF (see Table 5).

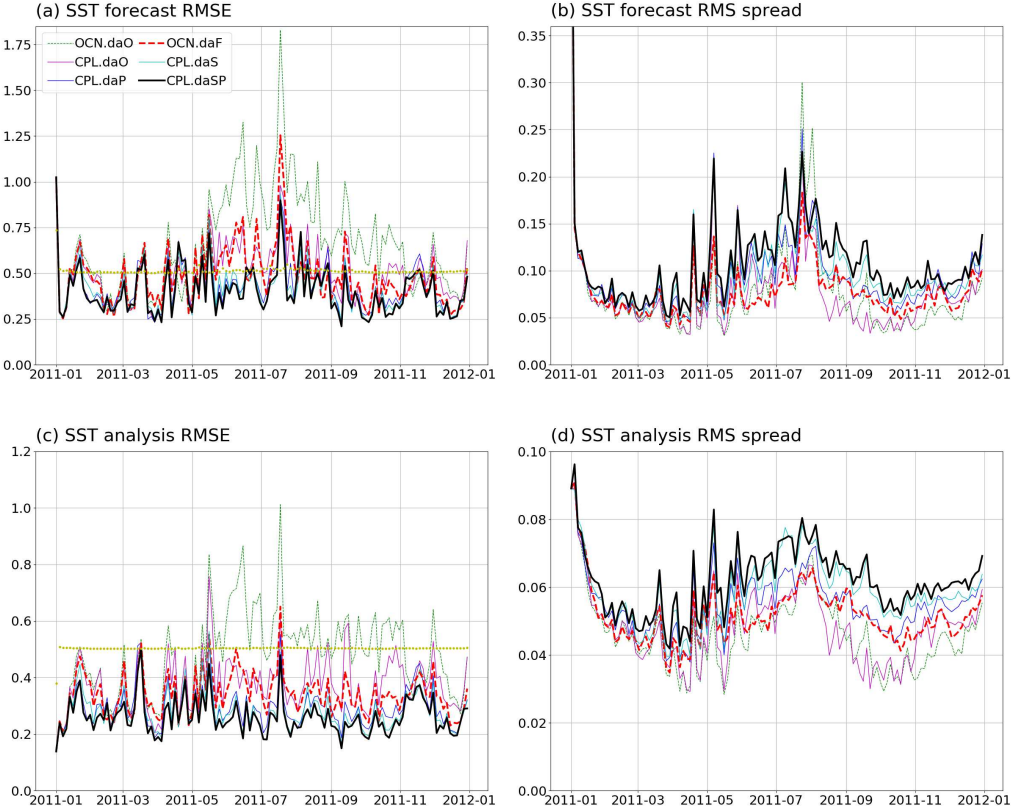


Figure 5. Time history of SST RMSEs and spreads during the data assimilation experiment. Panels (a) and (c) show the RMSEs of the forecasts and analyses against the assimilated data; Panels (b) and (d) show the spread of SST in the forecasts and analyses. The yellow dots in Panels (a) and (c) indicate the total uncertainty (square root of the sum of ensemble variance and observational variance (0.5°C) 2) of CPL.daSP.

380

3.4 Temperature and Salinity Profiles

381
382
383
384
385
386
387
388
389
390
391
392
393
394
395
396

The subsurface features of the ocean are validated against independent (i.e. not assimilated) CTD observations of temperature and salinity from the WHOI/KAUST summer cruise in the Red Sea between September 15 and October 08 2011. The difference between daily averaged forecasts and observations is shown in Figs. 9 and 10. More than 2 degree and 0.8 psu differences are found for temperature and salinity profiles in the thermocline between 50–100 m. For the temperature profiles, the RMSE in CPL.daSP (0.361°C) is smaller than OCN.daO (0.408°C) by about 10%, especially near the ocean surface, but within 2% difference compared to OCN.daF, CPL.daO, and CPL.daS. For the salinity profiles, the forecast RMSE of CPL.daSP (0.082 psu) is smaller than the benchmark experiment OCN.daO by about 30%. It is noted that CPL.daP has the smallest RMSE for temperature (0.344°C), but its salinity RMSE is significantly larger (0.122 psu) than CPL.daSP. Compared with the ocean-only experiment OCN.daF, the RMSEs in CPL.daS and CPL.daSP are not significantly different (within 1% or 2%). Although the coupled experiment is no better than the best uncoupled experiment OCN.daF, the results indicate the stochastic schemes in WRF are crucial for producing better forecasts of the ocean profiles.

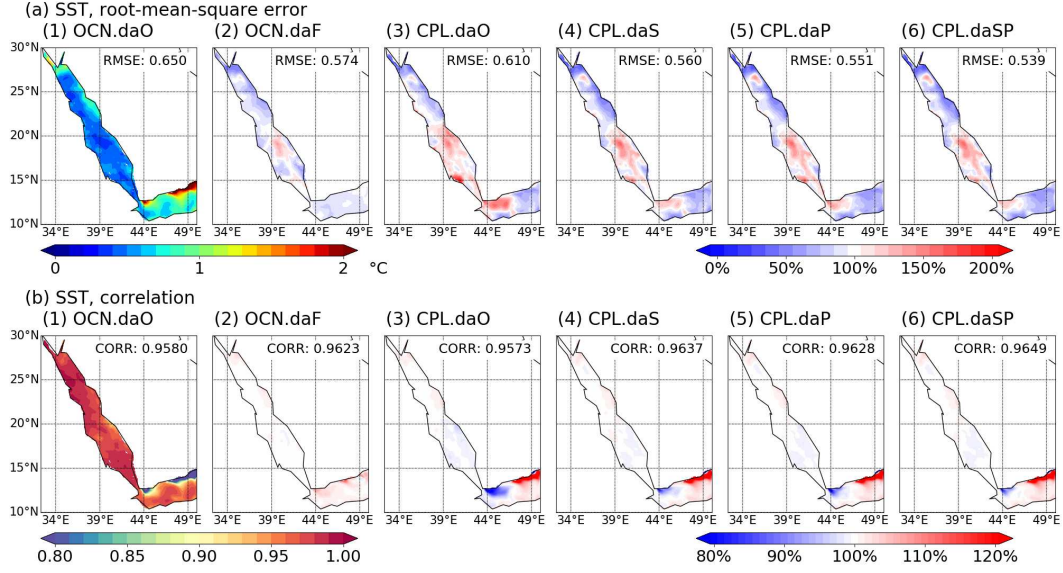


Figure 6. SST RMSEs and correlations obtained in the DA experiments validated against OSTIA. Panels (a) and (b) show the RMSE and correlation of the ‘forecast’ SST. The contours in column 1 indicate the comparison with OSTIA data; columns 2-5 are normalized by the reference OCN.daO in column 1 to highlight differences, showing the ratios in percentage.

Table 5. Summary of SSH against the validation data. We highlighted the best forecast/analysis using red, but the pink color is used when the differences between coupled and coupled experiments are insignificant (when the RMSE difference is smaller than 5% or the standard error).

	OCN.daO	OCN.daF	CPL.daO	CPL.daS	CPL.daP	CPL.daSP
Against assimilated data						
SSH forecast RMSE	0.0646	0.0626	0.0650	0.0624	0.0626	0.0620
SSH analysis RMSE	0.0580	0.0495	0.0578	0.0446	0.0522	0.0433
Against CMEMS-L4 SSH						
SSH forecast RMSE	0.0513	0.0486	0.0513	0.0483	0.0494	0.0482
SSH analysis RMSE	0.0461	0.0390	0.0455	0.0356	0.0409	0.0350
SSH forecast correlation	0.9121	0.9197	0.9109	0.9197	0.9168	0.9204
SSH analysis correlation	0.9314	0.9493	0.0320	0.9578	0.9439	0.9590
SSH forecast spread	0.0034	0.0056	0.0036	0.0073	0.0048	0.0076
SSH analysis spread	0.0023	0.0038	0.0024	0.0046	0.0032	0.0047

397

3.5 Feedback to the Atmosphere

To assess the impact of ocean data assimilation on the surface of the atmosphere, we compare the latent heat fluxes and 10-m wind speed obtained in the DA experiments. This analysis informs feedback to the heat and momentum fluxes. We consider ERA5 as reference and present the RMSEs of latent heat fluxes and 10-m wind speed in Fig. 11. Here we only compare the data on the centerline of the Red Sea to highlight ocean regions. It can be seen that the RMSEs do not grow significantly with time, showing the capability of the coupled system for the 1-year DA experiments. We hypothesize this is

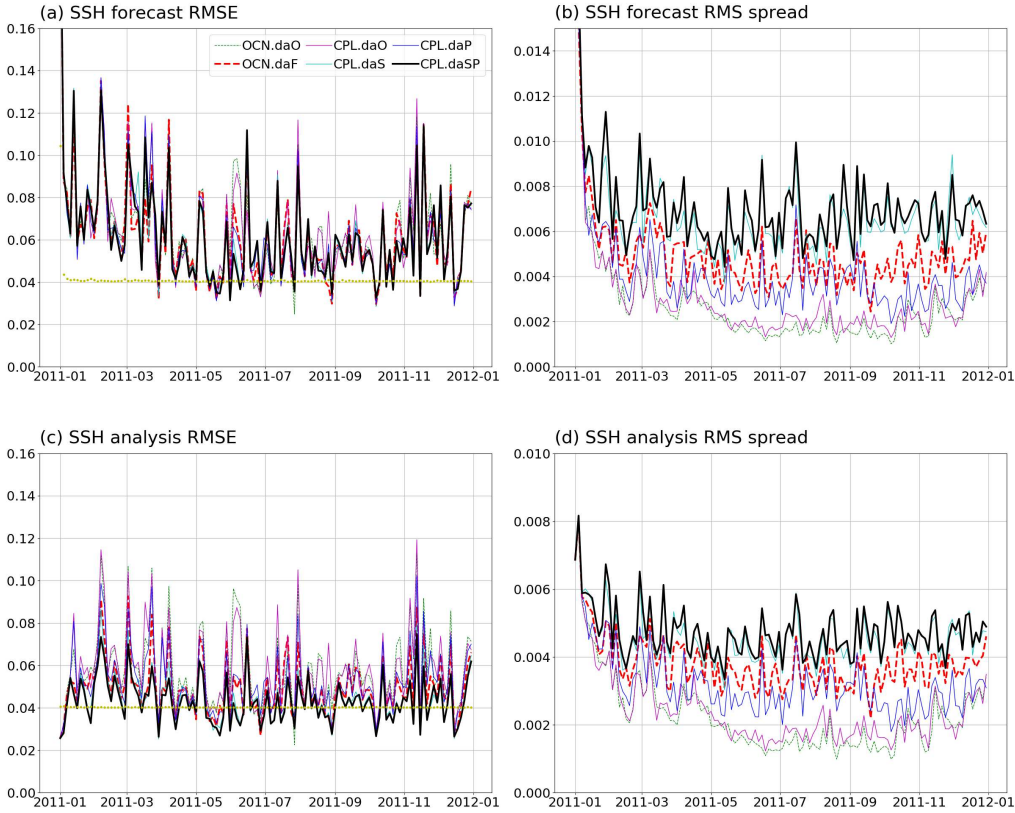


Figure 7. Evolution of the SSH RMSEs and spreads during the data assimilation experiment. Panels (a-b) show the RMSEs of the forecasts and analyses against the assimilated data; Panels (c-d) show the RMS spread of SSH in the forecasts and analyses. The yellow dots in Panels (a) and (c) indicate the total uncertainty (square root of the sum of ensemble variance and observational variance (0.04 m^2) of CPL.daSP.

405 because the atmospheric states are constrained by the boundary conditions for this
 406 relatively small domain. Compared with the RMSEs of latent heat flux and 10-m wind speed
 407 in the benchmark case CPL.daO (62.9 W/m^2 and 1.52 m/s), the CPL.daSP (60.2 W/m^2
 408 and 1.47 m/s) has smaller errors by about 4%, but the RMSE differences are smaller than
 409 the standard error (3.1 W/m^2 and 0.09 m/s), implying the improved ocean states may
 410 not significantly impact the atmospheric states. Because of the small differences in the
 411 surface atmosphere, this indicates that for the Red Sea region, the skill of the coupled
 412 model is not from the two-way coupling, but from the atmospheric forcings in the down-
 413 scaled WRF ensembles (one-way coupled) to drive the ocean model.

414 3.6 Vertical Current Velocity

415 Toye et al. (2017) argued that the dynamical balances (or assimilation shock) in
 416 the oceanic model from the EAKF increments increase the spread of the Red Sea fore-
 417 casts. The imbalances are also reported in other EAKF assimilation experiments (L. A. An-
 418 derson et al., 2000; Hoteit et al., 2010; Park et al., 2018). Here, we investigate the dy-
 419 namic balances in our experiments by comparing the standard deviation of $|w|$ obtained
 420 in the DA experiments with the “free” run without assimilating observation data in Fig. 12.
 421 The results show that the spreads of $|w|$ in all DA experiments are larger than the “free”
 422 run for the Red Sea region, but the changes in $|w|$ spread in CPL.daSP are close to the

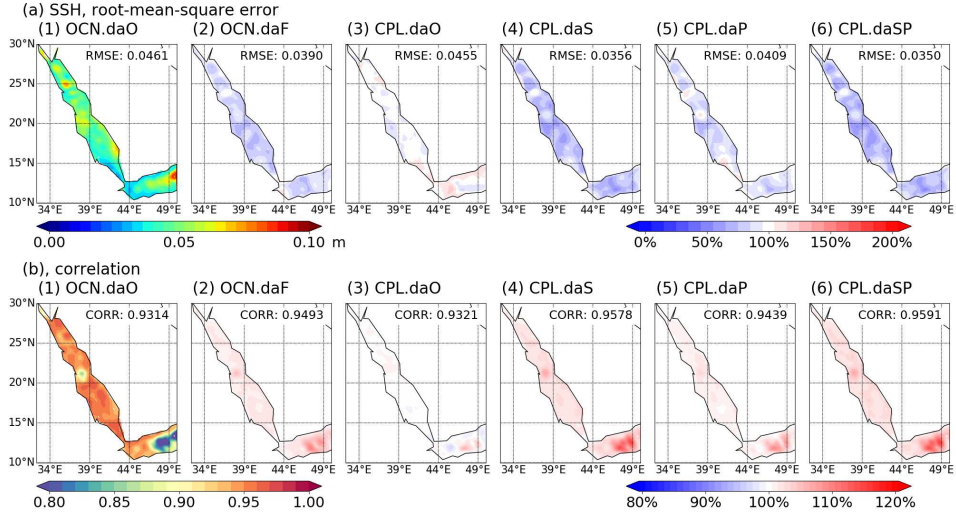


Figure 8. SSH RMSEs and correlations obtained in the DA experiments validated against CMEMS-L4 data. Panels (a) and (b) show the RMSEs and correlations of the SSH analyses. The contours in column 1 indicate the comparison with CMEMS-L4 data; columns 2-5 are normalized by the reference OCN.daO in column 1 to highlight differences, showing the ratios in percentage

423 ocean-only model experiment OCN.daF, indicating no significant dynamical imbalances
424 are introduced when using the coupled model.

4 Summary and Conclusions

426 This work implemented a data assimilation framework based on the regional coupled
427 model SKRIPS and DART. Using the EAKF in DART, we investigate the impact
428 of ocean data assimilation on the oceanic and atmospheric states of the Red Sea. The
429 coupled system assimilates satellite-based sea surface temperature and height and in situ
430 temperature and salinity glider profiles every 3 days for 1 year starting from January 01,
431 2011.

432 To assess the performance of the ensemble forecasts and examine the generated ocean
433 states, we ran a series of experiments using different perturbation schemes. The assimila-
434 tion results of the coupled experiments are compared with the uncoupled ones forced
435 by ECMWF-derived surface forcing, revealing that the coupled experiments give greater
436 spread in the ensembles of ocean states, with the spread continuing to increase when us-
437 ing the stochastic kinetic energy backscatter (SKEB) scheme. Compared with the as-
438 similated data, the coupled experiments result in a more skillful SST and SSH ensem-
439 ble mean forecast. The SST forecasts and SSH analyses in coupled models are also bet-
440 ter than uncoupled ones when compared with the independent observational data, but
441 the RMSEs of SST analyses and SSH forecasts are insignificantly different.

442 We further compared the DA experiment results with the independent cruise ob-
443 servation data of temperature and temperature profiles. The comparison shows large vari-
444 ations in the temperature profiles because of the challenge in modeling the thermocline
445 layer and the lack of in situ data. The RMSEs from the coupled DA experiments with
446 perturbations of the atmospheric model are comparable to the uncoupled model driven
447 by ECMWF-derived ensemble forcing, and both are better than the benchmark exper-
448 iments with small spreads in atmospheric forcings. To investigate the feedback from the
449 ocean, we validated the latent heat flux and 10 m winds in all coupled experiments us-
450 ing ERA5 data, but no significant difference is observed.

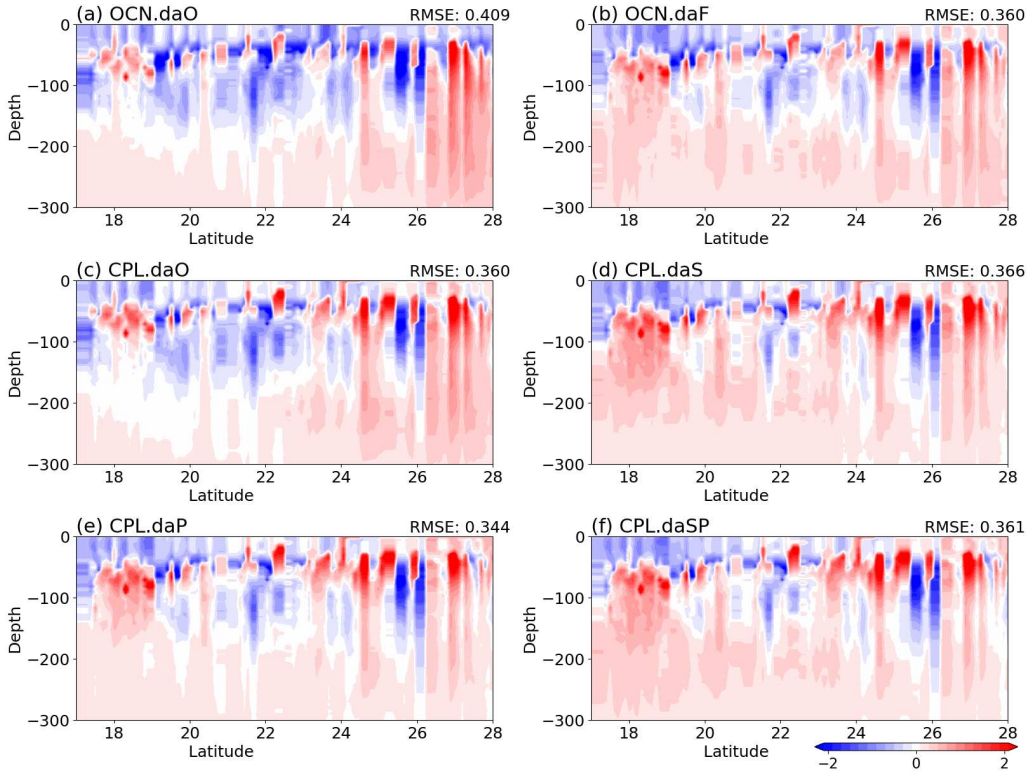


Figure 9. The differences between the temperature at 0–300 m obtained in the DA experiments compared to in situ observations (results minus observations).

This study demonstrates that our Red Sea DA system using two-way coupled model with WRF performs better or equal to an uncoupled model driven by ECMWF-derived ensemble surface forcing, showing a promising approach for forecasting the oceanic states or producing ocean analysis data. The dynamical imbalances in the coupled model are also not significantly different from the uncoupled model. The DA system implemented here explores the utility of a coupled DA system and studies of the ocean–atmosphere interactions using the analysis data.

Acknowledgments

We gratefully acknowledge the research funding (grant number: OSR-2022-NCM-4829.5) from KAUST (King Abdullah University of Science and Technology). We also appreciate the computational resources of the supercomputer Shaheen II and the assistance provided by KAUST Supercomputer Laboratory. RS and ACS were supported by ONR ASTRAL research initiative (N00014-23-1-2092). ACS was supported by NOAA Grant NA18OAR4310405 and ONR MISOBOP research initiative (N00014-17-S-B001). BDC and MRM were supported by NOAA Grant NA21OAR4310257, NA18OAR4310403, and NA22OAR4310597. AJM was partly supported by the National Science Foundation (OCE-2022868). We appreciate Luca Delle Monache, Daniel Steinhoff, and Rachel Weihs for discussing the generation of WRF ensembles.

Data Availability Statement

The coupled model used for the simulations is available at https://github.com/iurnus/scripps_kaust_model. The DA experimental results used in the paper are available at <https://zenodo.org/records/10408667>.

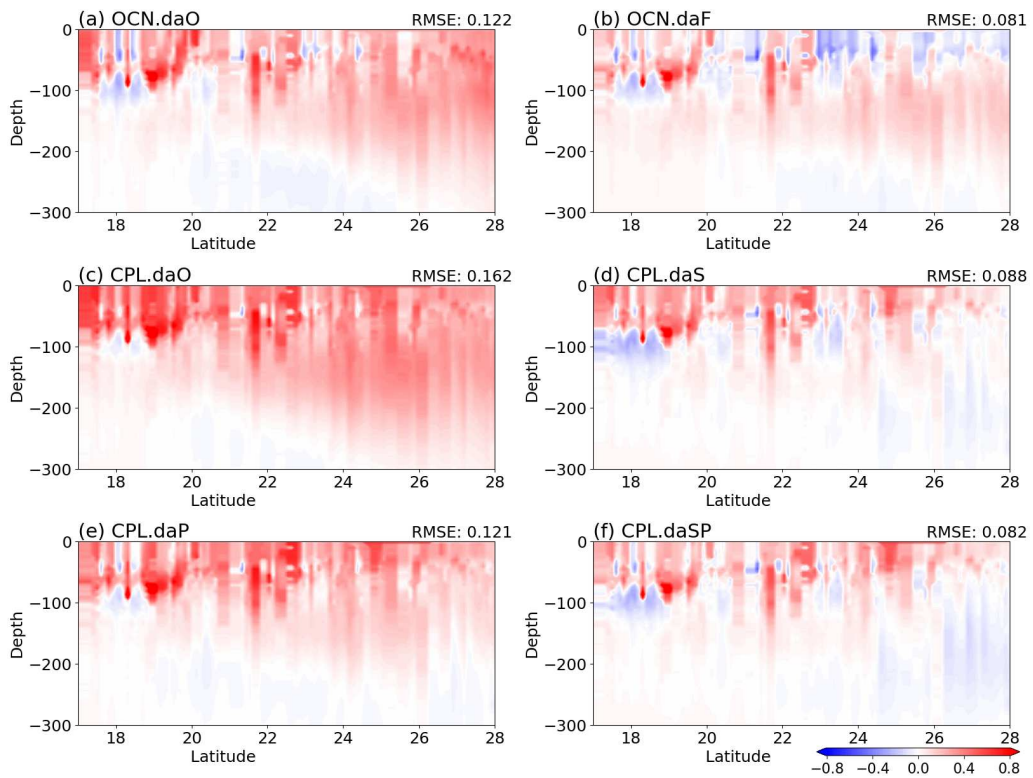


Figure 10. The differences between the salinity at 0-300 m obtained in the DA experiments in comparison with in situ observations (results minus observations).

473 Author contributions statement

474 All authors conceived the experiments; R.S. implemented the DA system for the
 475 coupled models; S.S. implemented the DA system for the uncoupled models and the RO-
 476 COTO workflow; R.S. conducted the experiments and plotted the figures; R.S. and S.S.
 477 drafted the initial manuscript; all authors discussed the results and revised the manuscript.

478 Competing Interests

479 The authors declare no competing interests.

480 References

481 Anderson, J., & Anderson, S. (1999). A Monte Carlo implementation of the nonlin-
 482 ear filtering problem to produce ensemble assimilations and forecasts. *Monthly*
 483 *Weather Review*, 127(12), 2741-2758. doi: 10.1175/1520-0493(1999)127<2741:
 484 AMCIOT>2.0.CO;2

485 Anderson, J., Hoar, T., Raeder, K., Liu, H., Collins, N., Torn, R., & Avellano, A.
 486 (2009). The Data Assimilation Research Testbed: A community facility. *Bul-*
 487 *letin of the American Meteorological Society*, 90(9), 1283–1296.

488 Anderson, L. A., Robinson, A. R., & Lozano, C. J. (2000). Physical and biological
 489 modeling in the Gulf Stream region: I. Data assimilation methodology. *Deep*
 490 *Sea Research Part I: Oceanographic Research Papers*, 47(10), 1787–1827.

491 Bannister, R. N. (2008a). A review of forecast error covariance statistics in at-
 492 mospheric variational data assimilation. I: Characteristics and measurements
 493 of forecast error covariances. *Quarterly Journal of the Royal Meteorological*
 494 *Society*, 134(637, B), 1951-1970. doi: 10.1002/qj.339

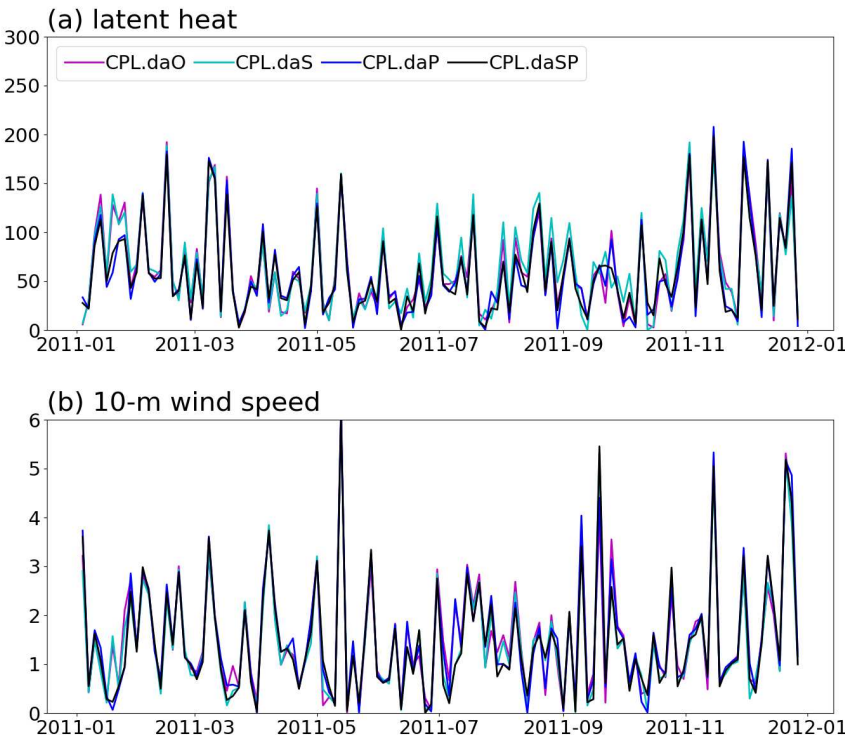


Figure 11. The RMSEs of latent heat flux and 10-m wind speed obtained in the coupled model when assimilating the ocean data. We only compare the data on the centerline of the Red Sea.

495 Bannister, R. N. (2008b). A review of forecast error covariance statistics in atmo-
 496 spheric variational data assimilation. II: Modelling the forecast error covariance
 497 statistics. *Quarterly Journal of the Royal Meteorological Society*, 134(637),
 498 1971–1996. doi: 10.1002/qj.340

499 Bannister, R. N. (2017). A review of operational methods of variational and
 500 ensemble-variational data assimilation. *Quarterly Journal of the Royal Me-
 501 teorological Society*, 143(703), 607–633.

502 Banzon, V., Smith, T. M., Chin, T. M., Liu, C., & Hankins, W. (2016). A long-term
 503 record of blended satellite and in situ sea-surface temperature for climate mon-
 504 itoring, modeling and environmental studies. *Earth System Science Data*, 8(1),
 505 165–176.

506 Berner, J., Fossell, K., Ha, S.-Y., Hacker, J., & Snyder, C. (2015). Increasing the
 507 skill of probabilistic forecasts: Understanding performance improvements from
 508 model-error representations. *Monthly Weather Review*, 143(4), 1295–1320.

509 Berner, J., Ha, S.-Y., Hacker, J., Fournier, A., & Snyder, C. (2011). Model un-
 510 certainty in a mesoscale ensemble prediction system: Stochastic versus multi-
 511 physics representations. *Monthly Weather Review*, 139(6), 1972–1995.

512 Berner, J., Shutts, G., Leutbecher, M., & Palmer, T. (2009). A spectral stochastic
 513 kinetic energy backscatter scheme and its impact on flow-dependent pre-
 514 dictability in the ECMWF ensemble prediction system. *Journal of the Atmo-
 515 spheric Sciences*, 66(3), 603–626.

516 Bougeault, P., Toth, Z., Bishop, C., Brown, B., Burridge, D., Chen, D. H., ... others
 517 (2010). The THORPEX interactive grand global ensemble. *Bulletin of the
 518 American Meteorological Society*, 91(8), 1059–1072.

519 Brankart, J.-M., Candille, G., Garnier, F., Calone, C., Melet, A., Bouttier, P.-A., ...
 520 Verron, J. (2015). A generic approach to explicit simulation of uncertainty in

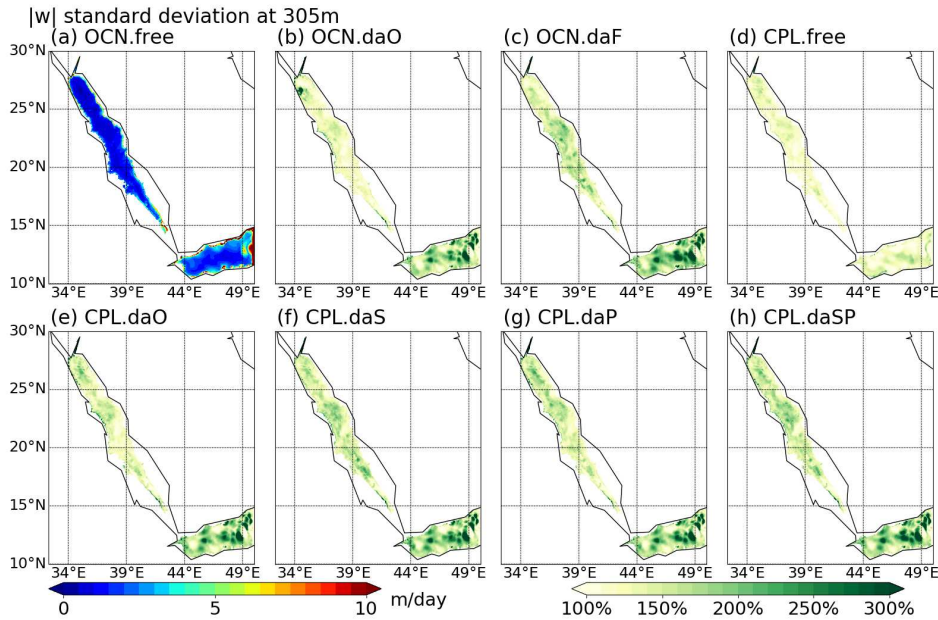


Figure 12. Standard deviation of $|w|$ at 300 m obtained in the DA experiments. Panels (b)-(h) are normalized by the reference OCN.free in panel (a) to highlight differences.

521 the NEMO ocean model. *Geoscientific Model Development*, 8(5), 1285-1297.
 522 doi: 10.5194/gmd-8-1285-2015

523 Buizza, R. (2014). *The TIGGE global, medium-range ensembles*. European Centre
 524 for Medium-Range Weather Forecasts.

525 Campin, J.-M., Heimbach, P., Losch, M., Forget, G., edhill3, Adcroft, A., ... T.,
 526 A. T. (2019). Mitgcm/mitgcm: checkpoint67m.
 527 doi: 10.5281/zenodo.3492298

528 Chen, S.-H., & Sun, W.-Y. (2002). A one-dimensional time dependent cloud model.
 529 *Journal of the Meteorological Society of Japan. Ser. II*, 80(1), 99–118.

530 Cox, M. (1987). Isopycnal diffusion in a z-coordinate ocean model. *Ocean modelling*,
 531 74, 1–5.

532 Danabasoglu, G., & McWilliams, J. (1995). Sensitivity of the global ocean circu-
 533 lation to parameterizations of mesoscale tracer transports. *Journal of Climate*,
 534 8(12), 2967–2987. doi: 10.1175/1520-0442(1995)008<2967:SOTGOC>2.0.CO;2

535 Dasari, H. P., Desamsetti, S., Langodan, S., Attada, R., Ashok, K., & Hoteit, I.
 536 (n.d.). Long-term changes in the Arabian Peninsula rainfall and their relation-
 537 ship with the ENSO signals in the tropical Indo-Pacific. *Climate Dynamics*,
 538 1–17.

539 Davis, S. R., Farrar, J. T., Weller, R. A., Jiang, H., & Pratt, L. J. (2019). The
 540 land-sea breeze of the Red Sea: observations, simulations, and relationships to
 541 regional moisture transport. *Journal of Geophysical Research: Atmospheres*,
 542 124(24), 13803–13825.

543 Donlon, C. J., Martin, M., Stark, J., Roberts-Jones, J., Fiedler, E., & Wimmer, W.
 544 (2012). The operational sea surface temperature and sea ice analysis (OSTIA)
 545 system. *Remote Sensing of Environment*, 116, 140–158.

546 Edwards, C. A., Moore, A. M., Hoteit, I., & Cornuelle, B. D. (2015). Re-
 547 gional ocean data assimilation. In C. Carlson & S. Giovannoni (Eds.),
 548 *Annual review of marine science*, vol 7 (Vol. 7, p. 21-42). doi: 10.1146/
 549 annurev-marine-010814-015821

550 Evensen, G. (1994). Sequential data assimilation with a nonlinear quasi-geostrophic
 551 model using Monte Carlo methods to forecast error statistics. *Journal of Geo-
 552 physical Research: Oceans*, 99(C5), 10143–10162.

553 Evensen, G. (2003). The ensemble Kalman filter: Theoretical formulation and practical implementation. *Ocean dynamics*, 53, 343–367.

554

555 Evensen, G. (2004). Sampling strategies and square root analysis schemes for the enkf. *Ocean Dynamics*, 54(6), 539-560. doi: 10.1007/s10236-004-0099-2

556

557 Evensen, G., & Van Leeuwen, P. J. (1996). Assimilation of Geosat altimeter data for the Agulhas current using the ensemble Kalman filter with a quasigeostrophic model. *Monthly Weather Review*, 124(1), 85–96.

558

559

560 Fairall, C., Bradley, E. F., Hare, J., Grachev, A., & Edson, J. (2003). Bulk parameterization of air-sea fluxes: Updates and verification for the COARE algorithm. *Journal of Climate*, 16(4), 571–591.

561

562

563 Gaspar, P., Gregoris, Y., & Lefevre, J. (1990). A simple eddy kinetic-energy model for simulations of the oceanic vertical mixing - Tests at station Papa and long-term upper ocean study site. *Journal of Geophysical Research-Oceans*, 95(C9), 16179-16193. doi: 10.1029/JC095iC09p16179

564

565

566

567 Gent, P., & Mcwilliams, J. (1990). Isopycnal mixing in ocean circulation models. *Journal of Physical Oceanography*, 20(1), 150-155. doi: 10.1175/1520-0485(1990)020<0150:IMOCM>2.0.CO;2

568

569

570 Gent, P., Willebrand, J., Mcdougall, T., & Mcwilliams, J. (1995). Parameterizing eddy-induced tracer transports in ocean circulation models. *Journal of Physical Oceanography*, 25(4), 463-474. doi: 10.1175/1520-0485(1995)025<0463:PEITTI>2.0.CO;2

571

572

573

574 Good, S. A., Martin, M. J., & Rayner, N. A. (2013). EN4: Quality controlled ocean temperature and salinity profiles and monthly objective analyses with uncertainty estimates. *Journal of Geophysical Research: Oceans*, 118(12), 6704–6716.

575

576

577

578 Grell, G. A., & Freitas, S. R. (2014). A scale and aerosol aware stochastic convective parameterization for weather and air quality modeling. *Atmospheric Chemistry and Physics*, 14(10), 5233–5250.

579

580

581 Griffies, S., & Hallberg, R. (2000). Biharmonic friction with a smagorinsky-like viscosity for use in large-scale eddy-permitting ocean models. *Monthly Weather Review*, 128(8, 2), 2935-2946. doi: 10.1175/1520-0493(2000)128<2935:BFWASL>2.0.CO;2

582

583

584

585 Harrop, C., samtrahan, christinaholt, & Brown, T. (2017, Sep). christopherwhar-
rop/rocoto: Rocoto 1.2.4.
586 doi: 10.5281/zenodo.890939

587

588 Hill, C., DeLuca, C., Balaji, Suarez, M., & Silva, A. (2004). The architecture of the earth system modeling framework. *Computing in Science & Engineering*, 6(1), 18–28.

589

590

591 Holland, W. (1978). Role of mesoscale eddies in general circulation of ocean - numerical experiments using a wind-driven quasi-geostrophic model. *Journal of Physical Oceanography*, 8(3), 363-392. doi: 10.1175/1520-0485(1978)008<0363:TROMEI>2.0.CO;2

592

593

594

595 Hong, S.-Y., & Lim, J.-O. J. (2006). The WRF single-moment 6-class microphysics scheme (WSM6). *Asia-Pacific Journal of Atmospheric Sciences*, 42(2), 129–151.

596

597

598 Hong, S.-Y., Noh, Y., & Dudhia, J. (2006). A new vertical diffusion package with an explicit treatment of entrainment processes. *Monthly Weather Review*, 134(9), 2318–2341.

599

600

601 Hoteit, I., Abualnaja, Y., Afzal, S., Ait-El-Fquih, B., Akylas, T., Antony, C., ...
602 Zodiatis, G. (2021). Towards an end-to-end analysis and prediction system for weather, climate, and marine applications in the Red Sea. *Bulletin of the American Meteorological Society*, 102(1), E99 - E122. Retrieved from <https://journals.ametsoc.org/view/journals/bams/102/1/BAMS-D-19-0005.1.xml> doi: <https://doi.org/10.1175/BAMS-D-19-0005.1>

603

604

605

606

607 Hoteit, I., Cornuelle, B., & Heimbach, P. (2010). An eddy-permitting, dynamically
 608 consistent adjoint-based assimilation system for the tropical Pacific: Hindcast
 609 experiments in 2000. *Journal of Geophysical Research: Oceans*, 115(C3).

610 Hoteit, I., Hoar, T., Gopalakrishnan, G., Collins, N., Anderson, J., Cornuelle, B.,
 611 ... Heimbach, P. (2013). A MITgcm/DART ensemble analysis and prediction
 612 system with application to the Gulf of Mexico. *Dynamics of Atmospheres and
 613 Oceans*, 63, 1–23.

614 Hoteit, I., Pham, D., & Blum, J. (2002). A simplified reduced order Kalman filtering
 615 and application to altimetric data assimilation in Tropical Pacific. *Journal
 616 of Marine Systems*, 36(1-2), 101-127. doi: 10.1016/S0924-7963(02)00129-X

617 Hoteit, I., Pham, D.-T., Gharamti, M., & Luo, X. (2015). Mitigating observa-
 618 tion perturbation sampling errors in the stochastic EnKF. *Monthly Weather
 619 Review*, 143(7), 2918–2936.

620 Houtekamer, P. L., Mitchell, H. L., Pellerin, G., Buehner, M., Charron, M., Spacek,
 621 L., & Hansen, B. (2005). Atmospheric data assimilation with an ensem-
 622 ble Kalman filter: Results with real observations. *Monthly Weather Review*,
 623 133(3), 604–620.

624 Iacono, M. J., Delamere, J. S., Mlawer, E. J., Shephard, M. W., Clough, S. A., &
 625 Collins, W. D. (2008). Radiative forcing by long-lived greenhouse gases: Cal-
 626 culations with the AER radiative transfer models. *Journal of Geophysical
 627 Research: Atmospheres*, 113(D13).

628 Ingleby, B., & Huddleston, M. (2007). Quality control of ocean temperature and
 629 salinity profiles—Historical and real-time data. *Journal of Marine Systems*,
 630 65(1-4), 158–175.

631 Janjić, Z. I. (1994). The step-mountain eta coordinate model: Further developments
 632 of the convection, viscous sublayer, and turbulence closure schemes. *Monthly
 633 Weather Review*, 122(5), 927–945.

634 Jean-Michel, L., Eric, G., Romain, B.-B., Gilles, G., Angélique, M., Marie, D., ...
 635 others (2021). The Copernicus global 1/12 oceanic and sea ice GLORYS12
 636 reanalysis. *Frontiers in Earth Science*, 9, 698876.

637 Kain, J. S. (2004). The kain–fritsch convective parameterization: an update. *Journal
 638 of applied meteorology*, 43(1), 170–181.

639 Karspeck, A. R., Yeager, S., Danabasoglu, G., Hoar, T., Collins, N., Raeder, K.,
 640 ... Tribbia, J. (2013). An ensemble adjustment Kalman filter for the
 641 CCSM4 ocean component. *Journal of Climate*, 26(19), 7392–7413. doi:
 642 10.1175/JCLI-D-12-00402.1

643 Kwon, K. M., Choi, B.-J., Lee, S.-H., Kim, Y. H., Seo, G.-H., & Cho, Y.-K. (2016).
 644 Effect of model error representation in the Yellow and East China Sea mod-
 645 eling system based on the ensemble Kalman filter. *Ocean Dynamics*, 66(2),
 646 263–283. doi: 10.1007/s10236-015-0909-8

647 Kwon, Y. C., & Hong, S.-Y. (2017). A mass-flux cumulus parameterization scheme
 648 across gray-zone resolutions. *Monthly Weather Review*, 145(2), 583–598.

649 Langodan, S., Cavalieri, L., Vishwanadhapalli, Y., Pomaro, A., Bertotti, L., &
 650 Hoteit, I. (2017). The climatology of the Red Sea—part 1: the wind. *Inter-
 651 national Journal of Climatology*, 37(13), 4509–4517.

652 Large, W., Danabasoglu, G., Doney, S., & McWilliams, J. (1997). Sensitivity to
 653 surface forcing and boundary layer mixing in a global ocean model: Annual-
 654 mean climatology. *Journal of Physical Oceanography*, 27(11), 2418–2447. doi:
 655 10.1175/1520-0485(1997)027<2418:STSFAB>2.0.CO;2

656 Large, W. G., McWilliams, J. C., & Doney, S. C. (1994). Oceanic vertical mixing: A
 657 review and a model with a nonlocal boundary layer parameterization. *Reviews
 658 of Geophysics*, 32(4), 363–403.

659 Lawson, W., & Hansen, J. (2004). Implications of stochastic and determinis-
 660 tic filters as ensemble-based data assimilation methods in varying regimes
 661 of error growth. *Monthly Weather Review*, 132(8), 1966–1981. doi:

662 10.1175/1520-0493(2004)132<1966:IOSADF>2.0.CO;2

663 Leeuwenburgh, O., Evensen, G., & Bertino, L. (2005). The impact of ensemble filter
664 definition on the assimilation of temperature profiles in the tropical Pacific.
665 *Quarterly Journal of the Royal Meteorological Society*, 131(613, C), 3291-3300.
666 doi: 10.1256/qj.05.90

667 Leith, C. (1996). Stochastic models of chaotic systems. *PHYSICA D*, 98(2-4),
668 481-491. (15th Annual International Conference of the Center-for-Nonlinear-
669 Studies on Nonlinear Phenomena in Ocean Dynamics, LOS ALAMOS, NM,
670 MAY 15-19, 1995) doi: 10.1016/0167-2789(96)00107-8

671 Lim, K.-S. S., & Hong, S.-Y. (2010). Development of an effective double-moment
672 cloud microphysics scheme with prognostic cloud condensation nuclei (CCN)
673 for weather and climate models. *Monthly Weather Review*, 138(5), 1587-1612.

674 Lima, L. N., Pezzi, L. P., Penny, S. G., & Tanajura, C. A. S. (2019). An investiga-
675 tion of ocean model uncertainties through ensemble forecast experiments in the
676 southwest Atlantic Ocean. *Journal of Geophysical Research-Oceans*, 124(1),
677 432-452. doi: 10.1029/2018JC013919

678 Lisæter, K. A., Rosanova, J., & Evensen, G. (2003). Assimilation of ice concen-
679 tration in a coupled ice-ocean model, using the ensemble Kalman filter. *Ocean
680 Dynamics*, 53(4), 368-388.

681 Liu, P., Tsimpidi, A., Hu, Y., Stone, B., Russell, A., & Nenes, A. (2012). Differences
682 between downscaling with spectral and grid nudging using WRF. *Atmospheric
683 Chemistry and Physics*, 12(8), 3601-3610.

684 Luo, X., & Hoteit, I. (2012). Ensemble Kalman filtering with residual nudging. *Tel-
685 lus A: Dynamic Meteorology and Oceanography*, 64(1), 17130.

686 Marshall, J., Adcroft, A., Hill, C., Perelman, L., & Heisey, C. (1997). A finite-
687 volume, incompressible Navier Stokes model for studies of the ocean on parallel
688 computers. *Journal of Geophysical Research: Oceans*, 102(C3), 5753-5766.

689 Mellor, G., & Yamada, T. (1982). Development of a turbulence closure-model for
690 geophysical fluid problems. *Reviews of Geophysics*, 20(4), 851-875. doi: 10
691 .1029/RG020i004p00851

692 Mertz, F., Rosmorduc, V., Maheu, C., & Faugére, Y. (2017). *Product user manual,
693 For sea level SLA products*.

694 Morrison, H., Thompson, G., & Tatarskii, V. (2009). Impact of cloud microphysics
695 on the development of trailing stratiform precipitation in a simulated squall
696 line: Comparison of one-and two-moment schemes. *Monthly Weather Review*,
697 137(3), 991-1007.

698 Nakanishi, M., & Niino, H. (2004). An improved Mellor-Yamada level-3 model with
699 condensation physics: Its design and verification. *Boundary-Layer Meteorology*,
700 112(1), 1-31.

701 Nakanishi, M., & Niino, H. (2009). Development of an improved turbulence closure
702 model for the atmospheric boundary layer. *Journal of the Meteorological Soci-
703 ety of Japan. Ser. II*, 87(5), 895-912.

704 Oakley, N. S., Liu, T., McGuire, L. A., Simpson, M., Hatchett, B. J., Tardy, A., ...
705 Steinhoff, D. (2023). Toward probabilistic post-fire debris-flow hazard decision
706 support. *Bulletin of the American Meteorological Society*.

707 Pacanowski, R., & Philander, S. (1981). Parameterization of vertical mixing in nu-
708 matical models of tropical oceans. *Journal of Physical Oceanography*, 11(11),
709 1443-1451.

710 Park, J.-Y., Stock, C. A., Yang, X., Dunne, J. P., Rosati, A., John, J., & Zhang, S.
711 (2018). Modeling global ocean biogeochemistry with physical data assimila-
712 tion: a pragmatic solution to the equatorial instability. *Journal of Advances in
713 Modeling Earth Systems*, 10(3), 891-906.

714 Penny, S. G., Behringer, D. W., Carton, J. A., & Kalnay, E. (2015). A hybrid global
715 ocean data assimilation system at NCEP. *Monthly Weather Review*, 143(11),
716 4660-4677. doi: 10.1175/MWR-D-14-00376.1

717 Prakash, P. J., Stenchikov, G., Kalenderski, S., Osipov, S., & Bangalath, H. (2014).
 718 The impact of dust storms on the Arabian Peninsula and the Red Sea. *Atmo-*
 719 *spheric Chemistry & Physics Discussions*, 14(13).

720 Redi, M. (1982). Oceanic isopycnal mixing by coordinate rotation. *Journal of Phys-*
 721 *ical Oceanography*, 12(10), 1154-1158. doi: 10.1175/1520-0485(1982)012(1154:OIMBCR)2.0.CO;2

723 Reynolds, R. W., Smith, T. M., Liu, C., Chelton, D. B., Casey, K. S., & Schlax,
 724 M. G. (2007). Daily high-resolution-blended analyses for sea surface tempera-
 725 ture. *Journal of climate*, 20(22), 5473-5496.

726 Sakov, P., Counillon, F., Bertino, L., Lisæter, K., Oke, P., & Koralev, A. (2012).
 727 Topaz4: an ocean-sea ice data assimilation system for the North Atlantic and
 728 Arctic. *Ocean Science*, 8(4), 633-656.

729 Sandery, P. A., Sakov, P., & Majewski, L. (2014). The impact of open boundary
 730 forcing on forecasting the east australian current using ensemble data assimila-
 731 tion. *Ocean Modelling*, 84, 1-11. doi: 10.1016/j.ocemod.2014.09.005

732 Sanikommu, S., Banerjee, D. S., Baduru, B., Paul, B., Paul, A., Chakraborty, K.,
 733 & Hoteit, I. (2019). Impact of dynamical representational errors on an in-
 734 dian ocean ensemble data assimilation system. *Quarterly Journal of the Royal*
 735 *Meteorological Society*, 145(725), 3680-3691.

736 Sanikommu, S., Langodan, S., Dasari, H. P., Zhan, P., Krokos, G., Abualnaja, Y. O.,
 737 ... Hoteit, I. (2023a). Making the case for high resolution regional ocean
 738 reanalyses: An example with the Red Sea. *Bulletin of the American Meteorol-*
 739 *ogical Society*, E1241-E1264.

740 Sanikommu, S., Langodan, S., Dasari, H. P., Zhan, P., Krokos, G., Abualnaja,
 741 Y. O., ... Hoteit, I. (2023b). Making the case for high-resolution regional
 742 ocean reanalyses: An example with the Red Sea. *Bulletin of the American*
 743 *Meteorological Society*, 104(7), E1241 - E1264. Retrieved from <https://journals.ametsoc.org/view/journals/bams/104/7/BAMS-D-21-0287.1.xml>
 744 doi: <https://doi.org/10.1175/BAMS-D-21-0287.1>

745 Sanikommu, S., Paul, A., Sluka, T., Ravichandran, M., & Kalnay, E. (2017). The
 746 pre-argo ocean reanalyses may be seriously affected by the spatial coverage of
 747 moored buoys. *SCIENTIFIC REPORTS*, 7. doi: 10.1038/srep46685

748 Sanikommu, S., Toye, H., Zhan, P., Langodan, S., Krokos, G., Knio, O., & Hoteit,
 749 I. (2020). Impact of atmospheric and model physics perturbations on a
 750 high-resolution ensemble data assimilation system of the Red Sea. *Journal of*
 751 *Geophysical Research: Oceans*, 125(8), e2019JC015611.

752 Shu, Y., Zhu, J., Wang, D., & Xiao, X. (2011). Assimilating remote sensing and
 753 in situ observations into a coastal model of northern South China Sea using
 754 ensemble Kalman filter. *Continental Shelf Research*, 31(6, S, SI), S24-S36. doi:
 755 10.1016/j.csr.2011.01.017

756 Shutts, G. (2005). A kinetic energy backscatter algorithm for use in ensemble pre-
 757 diction systems. *Quarterly Journal of the Royal Meteorological Society: A*
 758 *journal of the atmospheric sciences, applied meteorology and physical oceanog-*
 759 *raphy*, 131(612), 3079-3102.

760 Skamarock, W. C., Klemp, J. B., Dudhia, J., Gill, D. O., Liu, Z., Berner, J., ...
 761 others (2019). A description of the advanced research WRF model version
 762 4. *National Center for Atmospheric Research: Boulder, CO, USA*, 145(145),
 763 550.

764 Smagorinsky, J., Galperin, B., & Orszag, S. (1993). Large eddy simulation of com-
 765 plex engineering and geophysical flows. *Evolution of physical oceanography*, 3-
 766 36.

767 Song, H., Hoteit, I., Cornuelle, B. D., & Subramanian, A. C. (2010). An adap-
 768 tive approach to mitigate background covariance limitations in the ensemble
 769 Kalman filter. *Monthly Weather Review*, 138(7), 2825-2845.

770

771 Stark, J. D., Donlon, C. J., Martin, M. J., & McCulloch, M. E. (2007). OSTIA: An
 772 operational, high resolution, real time, global sea surface temperature analysis
 773 system. In *Oceans 2007-europe* (pp. 1–4).

774 Sun, R., Cobb, A., Villas Bôas, A. B., Langodan, S., Subramanian, A. C., Mazloff,
 775 M. R., ... Hoteit, I. (2023). Waves in SKRIPS: WAVEWATCH III coupling
 776 implementation and a case study of tropical cyclone mekunu. *Geoscientific
 777 Model Development*, 16(12), 3435–3458.

778 Sun, R., Subramanian, A. C., Miller, A. J., Mazloff, M. R., Hoteit, I., & Cornuelle,
 779 B. D. (2019). SKRIPS v1.0: a regional coupled ocean–atmosphere modeling
 780 framework (MITgcm–WRF) using ESMF/NUOPC, description and prelim-
 781 inary results for the Red Sea. *Geoscientific Model Development*, 12(10),
 782 4221–4244. doi: 10.5194/gmd-12-4221-2019

783 Tewari, M., Chen, F., Wang, W., Dudhia, J., LeMone, M., Mitchell, K., ... Cuenca,
 784 R. (2004). Implementation and verification of the unified NOAH land sur-
 785 face model in the WRF model. In *20th conference on weather analysis and
 786 forecasting/16th conference on numerical weather prediction* (Vol. 1115).

787 Thompson, G., Field, P. R., Rasmussen, R. M., & Hall, W. D. (2008). Explicit fore-
 788 casts of winter precipitation using an improved bulk microphysics scheme. Part
 789 II: Implementation of a new snow parameterization. *Monthly Weather Review*,
 790 136(12), 5095–5115.

791 Toye, H., Zhan, P., Gopalakrishnan, G., Kartadikaria, A. R., Huang, H., Knio, O.,
 792 & Hoteit, I. (2017). Ensemble data assimilation in the Red Sea: sensitivity to
 793 ensemble selection and atmospheric forcing. *Ocean Dynamics*, 67(7), 915–933.
 794 doi: 10.1007/s10236-017-1064-1

795 Vandenbulcke, L., & Barth, A. (2015). A stochastic operational forecasting system
 796 of the Black Sea: Technique and validation. *Ocean Modelling*, 93, 7–21. doi: 10
 797 .1016/j.ocemod.2015.07.010

798 Wan, L., Zhu, J., Bertino, L., & Wang, H. (2008). Initial ensemble generation and
 799 validation for ocean data assimilation using HYCOM in the Pacific. *Ocean Dy-
 800 namics*, 58, 81–99.

801 Whitaker, J. S., & Hamill, T. M. (2012). Evaluating methods to account for system
 802 errors in ensemble data assimilation. *Monthly Weather Review*, 140(9), 3078–
 803 3089. doi: 10.1175/MWR-D-11-00276.1

804 Zhai, P., Bower, A. S., Smethie Jr, W. M., & Pratt, L. J. (2015). Formation and
 805 spreading of Red Sea outflow water in the Red Sea. *Journal of Geophysical Re-
 806 search: Oceans*, 120(9), 6542–6563.

807 Zhang, C., & Wang, Y. (2017). Projected future changes of tropical cyclone activity
 808 over the western North and South Pacific in a 20-km-mesh regional climate
 809 model. *Journal of Climate*, 30(15), 5923–5941.

810 Zhang, F., Snyder, C., & Sun, J. (2004). Impacts of initial estimate and ob-
 811 servation availability on convective-scale data assimilation with an ensem-
 812 ble Kalman filter. *Monthly Weather Review*, 132(5), 1238–1253. doi:
 813 10.1175/1520-0493(2004)132<1238:IOIEAO>2.0.CO;2